

Models of helically symmetric binary systems

Shin'ichirou Yoshida^{1,4}, Benjamin C. Bromley², Jocelyn S. Read¹, Kōji Uryū^{1,3}, and John L. Friedman¹

¹ Department of Physics, University of Wisconsin-Milwaukee, P.O. Box 413, Milwaukee, WI 53201, U.S.

² Department of Physics, University of Utah, Salt Lake City, Utah 84112, U.S.

³ SISSA, via Beirut 4, 34014 Trieste, Italy

⁴ Department of Physics, Florida Atlantic University, Boca Raton FL 33431, U.S.

E-mail: jsread@uwm.edu

Abstract. Results from helically symmetric scalar field models and first results from a convergent helically symmetric binary neutron star code are reported here; these are models stationary in the rotating frame of a source with constant angular velocity Ω . In the scalar field models and the neutron star code, helical symmetry leads to a system of mixed elliptic-hyperbolic character. The scalar field models involve nonlinear terms of the form ψ^3 , $(\nabla\psi)^2$, and $\psi\Box\psi$ that mimic nonlinear terms of the Einstein equation. Convergence is strikingly different for different signs of each nonlinear term; it is typically insensitive to the iterative method used; and it improves with an outer boundary in the near zone. In the neutron star code, one has no control on the sign of the source, and convergence has been achieved only for an outer boundary less than ~ 1 wavelength from the source or for a code that imposes helical symmetry only inside a near zone of that size. The inaccuracy of helically symmetric solutions with appropriate boundary conditions should be comparable to the inaccuracy of a waveless formalism that neglects gravitational waves; and the (near zone) solutions we obtain for waveless and helically symmetric BNS codes with the same boundary conditions nearly coincide.

1. Introduction

Initial data for the inspiral of binary neutron star (BNS) systems and corresponding quasiequilibrium BNS models have been based either on the initial value equations alone or on the IWM (Isenberg-Wilson-Mathews) spatially conformally flat ansatz. In each case one solves a truncated version of the Einstein equation for a metric having fewer than the six independent potentials that remain after a choice of gauge. The error of the approximation limits the accuracy of the first orbits of simulations in two ways: The initial data has spurious radiation; and, more importantly, the balance between gravitational attraction and orbital acceleration is not enforced, leading to orbits that are not exactly circular.

One way to go beyond spatial conformal flatness is to construct an analog in the full theory of the Newtonian binaries that are stationary in a rotating frame. In general relativity, these models are helically symmetric spacetimes [1, 2], with equal amounts of ingoing and outgoing radiation. Binary black holes of this kind were first discussed by Blackburn and Detweiler [3], and models involving nonlinear scalar wave equations have been studied by a group of researchers organized by Price (henceforth the *Consortium*) [4, 5, 6, 7, 8, 9]. Because the power radiated by a helically symmetric binary is constant in time, the spacetime cannot be asymptotically flat. At distances large compared to $1/\Omega$, however, the spacetime of a binary system with a helical Killing vector approximates asymptotic flatness – until, beyond about $10^4 M$ for neutron-star models of mass M , the enclosed energy in gravitational waves is comparable to the mass of the binary. The approximation is similar to, and possibly more accurate than, a 3rd post-Newtonian approximation in which the 2 1/2 post-Newtonian radiation is omitted.

In this paper, we report the construction of a convergent neutron-star code in which the full Einstein equation, together with the equation of hydrostatic equilibrium, is solved numerically under the assumption of helical symmetry. Convergence relies on a boundary that is not much farther than a wavelength from the system, and we present results from a number of related nonlinear scalar field models in which convergence requires either a small coefficient of the nonlinear term or a boundary close to the source. The results of these toy models are surprising in two ways. First, convergence of the scalar-field models is most strongly affected by the sign of the source term, with one choice of sign yielding a convergent solution for remarkably large values of the nonlinear terms we examined. Second, convergence does not depend strongly on the iterative method used to solve the equation, on whether one uses, for example, a Newton-Raphson iteration or an iteration based on a Green function that inverts only a convenient part of the second-order nonlinear operator.

The plan of the paper is as follows. Sect. 2 introduces the set of toy scalar field models with nonlinear terms chosen to mimic the nonlinear terms in the dynamical part of the Einstein equation. We describe several iteration methods, one closely related to that of the Uryu code, the others to codes developed by Andrade *et. al.* in [7] and further by Bromley, Owen, and Price [9]. Sect. 3 compares the accuracy of codes based on the various iteration methods. Sect. 4 reports the main results on convergence of the scalar-field models. Finally, Sect. 6 describes Uryu’s neutron-star code, presents its first results, and compares the solution it yields to that of a closely related code based on a waveless formalism [10].

2. Toy Problems

2.1. Helically symmetric, nonlinear scalar wave equations

We consider a scalar field ψ on Minkowski space, satisfying a wave equation with a source s that mimics two objects in circular orbit and with a nonlinear term $\mathcal{N}[\psi]$, whose strength is adjusted by a coefficient λ :

$$\square\psi - \lambda\mathcal{N}[\psi] = s. \quad (1)$$

We use three different nonlinear terms: $\mathcal{N}[\psi] = \psi^3$, $\mathcal{N}[\psi] = |\nabla\psi|^2$ with ∇ the spatial gradient, and $\mathcal{N}[\psi] = \psi\square\psi$, chosen to represent the types of nonlinear terms that appear in dynamical components of the field equations.

The source s is a sum of two 3-dimensional gaussian distributions,

$$s(t, r, \theta, \phi) = \sum_{\pm} \frac{q}{\sqrt{(2\pi)^3}} \exp\left(-\frac{(\vec{r} \pm \vec{R}(t))^2}{\sigma^2}\right), \quad (2)$$

centered about points $\pm\mathbf{R}$, $\mathbf{R}(t) = a[\cos(\Omega t)\hat{\mathbf{x}} + \sin(\Omega t)\hat{\mathbf{y}}]$, each a distance a from the origin and each having spread σ^2 and total charge q . The source s is stationary in a frame moving with angular velocity Ω ; that is, it is Lie-derived by the helical Killing vector

$$k^\alpha = t^\alpha + \Omega\phi^\alpha \quad (3)$$

of Minkowski space, where t^α and ϕ^α (equivalently ∂_t and ∂_ϕ) are generators of time-translations and of rotations in the plane of the binary source.

One can regard the scalar-field models as toy models of neutron stars of mass M , if the charge q of each gaussian source is identified with $4\pi M$. In gravitational units ($G=c=1$), all quantities of a binary star system can be specified in terms of M . In the models presented below, we set $q = 1$, $a = 1$, $\sigma = 0.5$, and $\Omega = 0.3$, corresponding to a binary system of mass M , stellar separation $2a = 8\pi M$, stellar radius $\sigma = 2\pi M$, and velocity $v = a\Omega = 0.3$.

A helically symmetric solution, like a genuinely stationary solution, is given by its value on a spacelike slice and the field equation (1) can be written in a form that involves only spatial derivatives. That is, using the symmetry relation $\mathcal{L}_k\psi = (\partial_t + \Omega\partial_\phi)\psi = 0$ to replace time derivatives by ϕ derivatives, one can rewrite Eq. (1) at $t = 0$ in the spatial form,

$$(\nabla^2 - \Omega^2\partial_\phi^2)\Psi - \lambda\mathcal{N}[\Psi] = S, \quad (4)$$

where $\Psi(r, \theta, \phi) = \psi(t = 0, r, \theta, \phi)$, $S(r, \theta, \phi) = s(t = 0, r, \theta, \phi)$. Then $\psi(t, r, \theta, \phi) = \Psi(r, \theta, \phi - \Omega t)$.

The operator $\mathcal{L} := \nabla^2 - \Omega^2\partial_\phi^2$ has a mixed character, elliptic inside the light cylinder $\Omega\sqrt{x^2 + y^2} = 1$, hyperbolic outside. The difficulties in finding numerical solutions stem from this behavior. In finding an iterative solution, one inverts the operator \mathcal{L} , but \mathcal{L} is not negative, and it lacks the contraction property that underlies the convergence of iterative schemes used to invert nonlinear elliptic equations and to prove existence of exact solutions.

2.2. Numerical methods

KEH method

In the KEH method one splits off the linear, flat-space operator \mathcal{L} and inverts it by a choice \mathcal{L}^{-1} of Green function. The iterative solution, beginning with $\Psi_0 = \mathcal{L}^{-1}S$, is then given by

$$\Psi_{n+1} = \Psi_0 + \lambda \mathcal{L}^{-1} \mathcal{N}[\Psi_n] \quad (5)$$

Although \mathcal{L} is not elliptic, the operator associated with each spherical harmonic is the elliptic Helmholtz operator: $\mathcal{L}[\Psi_{lm}(r)Y_{lm}] = [\nabla^2 + m^2\Omega^2][\Psi_{lm}(r)Y_{lm}]$. The corresponding radial operator $\frac{d^2}{dr^2} + \frac{2}{r} \frac{d}{dr} - \frac{l(l+1)}{r^2} + m^2\Omega^2$ has as its eigenfunctions the spherical Bessel functions, from which a Green function is constructed. For definiteness, we choose as \mathcal{L}^{-1} the form that, for a bounded source, yields the half-advanced+half-retarded solution, namely

$$\mathcal{L}^{-1}S := \sum_{lm} \int dr' S_{lm}(r') g_{lm}(r, r') Y_{lm}(\theta, \phi), \quad (6)$$

with

$$g_{l0} = \frac{1}{2l+1} \frac{r_{<}^l}{r_{>}^{l+1}}, \quad g_{lm} = m\Omega j_l(m\Omega r_{<}) n_l(m\Omega r_{>}), \quad m \neq 0. \quad (7)$$

Here $r_{<} = \min(r, r')$, $r_{>} = \max(r, r')$, and $j_l(x)$ and $n_l(x)$ are the spherical Bessel functions of the first and second kinds.

At each iteration, the nonlinear term $\mathcal{N}[\Psi_n]$ serves as an effective source. The polynomial nonlinear function Ψ^3 is most easily computed by shifting from $\Psi_{lm}(r)$ back into $\Psi(r, \theta, \phi)$ and cubing at each point, while the derivative-based nonlinear terms, $|\nabla\Psi|^2$ and $\Psi\nabla^2\Psi$, are calculated using the properties of the spherical harmonics.

Finally, as is usual in codes to solve nonlinear elliptic equations, we use softening and continuation to extend the range of convergence to larger values of λ . That is, instead of using Ψ_{n+1} as defined in Eq. (5), we can use a softened Ψ_{n+1}^ω defined by

$$\Psi_{n+1}^\omega = \omega \Psi_{n+1} + (1 - \omega) \Psi_n. \quad (8)$$

Given a converged field solution for some nonlinearity with small λ , it is sometimes possible to use continuation to obtain a solution for larger λ : The converged solution to Eq. (4) with weak nonlinearity is used as the initial field Ψ_0 for the iteration of Eq. (5) for strong nonlinearity. In this way one moves along a sequence of solutions with increasing values of λ . The effectiveness of softening and convergence is explored in Section 4.

Finite difference and eigenspectral methods

The Finite Difference code uses an iteration based on the Newton-Raphson method, with numerical approximations that reduce it in part to a secant method. Write the equation to be solved as

$$F = \mathcal{L}\Psi - \lambda \mathcal{N}[\Psi] - S = 0. \quad (9)$$

Numerically, Ψ is given by a set of values Ψ_i on the three-dimensional spatial slice. Given an initial field Ψ_i , each iterative step generates a modification $\delta\Psi_i$ by inverting

$$J_{ij} \delta\Psi_j = -F_i \quad (10)$$

where J_{ij} is the Jacobian

$$J_{ij} = \frac{\partial F_i}{\partial \Psi_j} \quad (11)$$

The Helmholtz operator has the form $(\mathcal{L}\Psi)_i = L_{ij}\Psi_j$ where L_{ij} is constructed from finite difference operations and incorporates boundary conditions. The corresponding part of J_{ij} is simple.

$$J_{ij} = \frac{\partial}{\partial \Psi_j} [L_{ik}\Psi_k - \lambda(\mathcal{N}[\Psi])_i - S_i] \quad (12)$$

$$= L_{ij} - \lambda \frac{\partial \mathcal{N}[\Psi]_i}{\partial \Psi_j} \quad (13)$$

The nonlinear piece of the Jacobian is evaluated numerically by varying local field values.

The Eigenspectral code [9] uses the same iterative scheme as the Finite Difference method, but it employs adapted coordinates and a discretized spectral decomposition. To specify the adapted coordinate system, we begin with comoving Cartesian coordinates $(\tilde{x}, \tilde{y}, \tilde{z})$ where the \tilde{z} -axis is the axis of rotation. The axes are rotated to a set

$$\tilde{X} = \tilde{y}, \tilde{Y} = \tilde{z}, \tilde{Z} = \tilde{x} \quad (14)$$

for which the \tilde{Z} -axis is a line through the center of each source. The adapted coordinates are chosen to approach spherical polar coordinates, with Θ measured from the \tilde{Z} axis, far from the sources. For each point $(\tilde{X}, \tilde{Y}, \tilde{Z})$, let r_1 and r_2 be the distances from the source centers, θ_1 and θ_2 corresponding angles from the \tilde{Z} axis. Then,

$$r_1 = \sqrt{(\tilde{Z} - a)^2 + \tilde{X}^2 + \tilde{Y}^2}, \quad (15)$$

$$r_2 = \sqrt{(\tilde{Z} + a)^2 + \tilde{X}^2 + \tilde{Y}^2}. \quad (16)$$

The adapted coordinates are

$$\chi = \sqrt{r_1 r_2} \quad (17)$$

$$\Theta = \frac{1}{2}(\theta_1 + \theta_2) = \frac{1}{2} \tan^{-1} \left(\frac{2\tilde{Z}\sqrt{\tilde{X}^2 + \tilde{Y}^2}}{\tilde{Z}^2 - a^2 - \tilde{X}^2 - \tilde{Y}^2} \right) \quad (18)$$

$$\Phi = \tan^{-1}(\tilde{X}/\tilde{Y}) \quad (19)$$

The spectral decomposition involves the angular Laplacian of Θ and Φ ,

$$D^2\Phi := \frac{1}{\sin\Theta} \frac{\partial}{\partial\Theta} \left[\sin\Theta \frac{\partial}{\partial\Theta} \right] + \frac{1}{(\sin\Theta)^2} \frac{\partial^2}{\partial\Phi^2}; \quad (20)$$

note that D^2 is *not* the angular part of ∇^2 in adapted coordinates, but it agrees asymptotically with the usual angular Laplacian far from the source. Instead of the spherical harmonics of the continuum Laplacian D^2 , the eigenspectral code uses the exact eigenvectors of the matrix L obtained by discretizing D^2 on the adapted coordinate grid $\{\Theta_i, \Phi_j\}$. Angular derivatives are represented in L by second order finite differencing. That is, with $[\sin\Theta D^2\Phi](\Theta_a, \Phi_b)$ approximated by $\sum_{ij} L_{ab,ij}\Psi(\Theta_i, \Phi_j)$,

the normalized eigenvectors $Y_{ij}^{(k)}$ of L satisfy

$$\sum_{ij} L_{ab,ij} Y_{ij}^{(k)} = -\Lambda^{(k)} \sin\Theta_a Y_{ab}^{(k)}, \quad (21)$$

$$\sum_{ij} Y_{ij}^{(k)} Y_{ij}^{(k')} \sin \Theta_i \Delta \Theta \Delta \Phi = \delta_{kk'}. \quad (22)$$

With the field expanded in terms of the eigenvectors $Y_{ij}^{(k)}$,

$$\Psi(\chi, \Theta_i, \Phi_j) = \sum_k a^{(k)}(\chi) Y_{ij}^{(k)}, \quad (23)$$

and the operator \mathcal{L} written in terms of adapted coordinates (Eq. 8-17 of [9]), $\mathcal{L}\Psi$ is expressed in terms of the $Y_{ij}^{(k)}$ (Eq. 31 of [9]),

$$\sum_k \left(\alpha_{k',k} \frac{d^2 a^{(k)}(\chi)}{d\chi^2} + \beta_{k',k} a^{(k)}(\chi) + \gamma_{k',k} \frac{da^{(k)}(\chi)}{d\chi} \right) = S_{k'}, \quad (24)$$

where the $\alpha_{k',k}$, $\beta_{k',k}$, and $\gamma_{k',k}$ involve angular derivatives of the $Y^{(k)}$ computed by finite differencing (Eqs. 41-43 of [9]). This equation for $a^{(k)}$ is iterated in the same fashion as in the Finite Difference method to find the solution with nonlinear terms.

If all harmonics were retained, the Eigenspectral method would be the equivalent of the Finite Difference method in adapted coordinates, although in a different basis. The advantage of the adapted coordinates is that the distribution of points encodes most of the physically relevant information in the low-order harmonics. Its disadvantage is that higher order harmonics require an increasingly cumbersome formalism. The code is consequently limited to harmonics $l \leq 2$, saving enough memory to allow high resolution in the radial coordinate.

2.3. Boundary conditions

The KEH method at each iteration finds a solution that has standing wave behaviour for the flat space piece, imposing boundary conditions by the choice of Green function. There remains freedom to add a homogeneous solution at each iteration, and this has been used to study the sensitivity of convergence to the choice of boundary condition.

The Eigenspectral and Finite Difference methods include boundary conditions in the finite difference matrix for the linear \square operator. Outgoing conditions are imposed on the edges of the grid by enforcing

$$(\partial_r \Psi - \partial_\phi \Psi)_{r=r_{\max}} = 0 \quad (25)$$

A solution for ingoing radiation can then be generated by a spatial inversion across the plane through the sources and perpendicular to their rotation. At each step, a periodic solution is constructed by superposition of the ingoing and outgoing solutions.

3. Estimating numerical accuracy

3.1. KEH code

Several types of numerical approximation in the KEH code produce effects that can be estimated by convergence testing. Most obvious is the choice of spatial grid in (r, θ, ϕ) on which numerical integration is performed. Very high resolution in θ and ϕ is easily obtained. The number of radial points is more problematic with our simple equispaced grids. A Richardson extrapolation error estimate from varying radial grid spacing shows that precision of 10^{-5} is estimated for runs comparing code results. Estimation of the range of λ giving convergent solutions is done at lower radial precision.

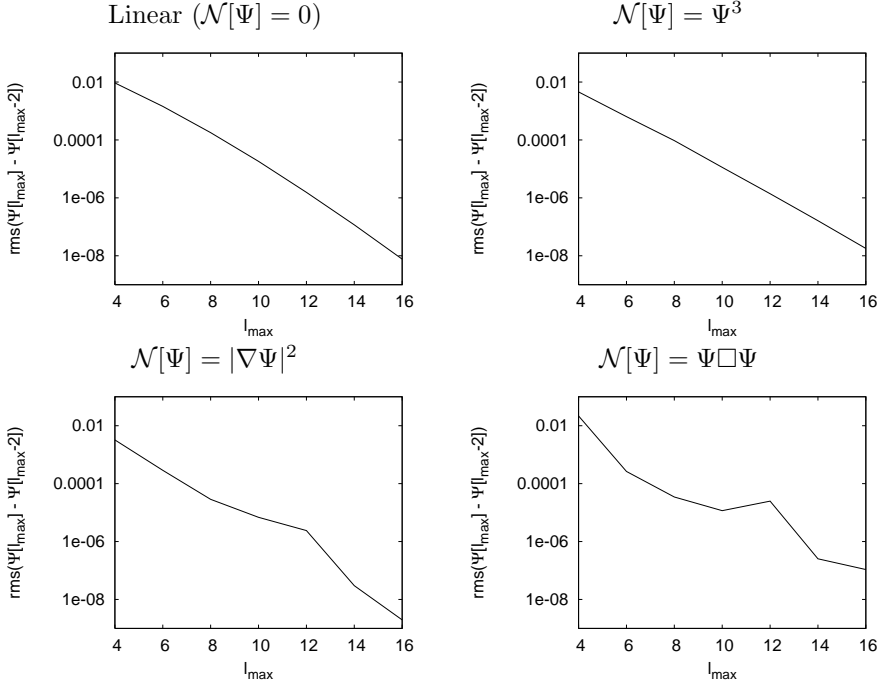


Figure 1. The rms change in the converged field as the number of harmonics considered increases.

As the KEH method rests on the decomposition of the field into spherical harmonics, accuracy will depend on the number of harmonics retained in the numerical calculation. Examining the difference between results with an increasing number of harmonics retained shows that a good approximation is to use up to $l = 12$ in the code. The fractional difference between the field calculated with $l_{\max} = 12$ and the field including higher harmonics is less than 10^{-6} at each point. Figure 1 displays the rms difference in solutions as the number of harmonics retained by the code is increased.

In the toy models presented below, a solution is computed at each iteration using the half-advanced+half-retarded Green function (6). Because the linear field Ψ of a perpetually radiating source falls off like r^{-1} , the nonlinear terms $\mathcal{N} = (\nabla\Psi)^2$ and $\mathcal{N} = \Psi\Box\Psi$ that serve as effective sources for each iteration do not fall off fast enough for the integrals to converge, if the outer boundary extends to infinity. One can, however, pick out a solution that is independent of the outer boundary by fixing the value of Ψ at a finite radius R . That is, one can, at each iteration, add the homogeneous solution that maintains the specified value of Ψ at R . This has remarkably little effect on the field in the region close to the sources, with less than a 1% change in field strength for points with $r < 6$. This insensitivity of the near-zone field to the amplitude of the waves, when the source dominates the solution, is the reason a helically symmetric solution makes sense as an approximation to an outgoing solution.

3.2. Comparing codes

With different 3D grid patterns for the codes, it is most straightforward to compare results on rays through the volume of interest. We compare the results extrapolated to three orthogonal axes: taking the x -axis through the centers of the two sources and the z -axis perpendicular to the plane of rotation. Both x and y axes show wave behaviour away from the sources; along the z axis, ψ shows only Coulomb-type behavior, because Y_{lm} vanishes on the axis when $m \neq 0$, and for $m = 0$, $\mathcal{L}\psi = \nabla^2\psi$.

Sample comparison plots are shown in Figure 2. Further comparisons are shown in the longer version of this paper on the gr-qc archive.

The field values on the axes are interpolated for comparison. Differences between fields are divided by the average field value of the three codes to find relative error, as plotted in the insets of Figure 2. We compute the rms of this relative error for the grid points along each axis. These rms values are expressed as percentages in Table 1. In the worst case, the rms difference is 3% between codes.

A smaller rms difference on the rotation axis than on the source and perpendicular axes indicates that discrepancies in the wave region dominate, as in the FD-KEH comparison with $\mathcal{N}[\Psi] = \Psi^3$, $\lambda = 100$. In other cases, the error on all three axes is comparable, and there is some shift between codes seen even on the rotation axis, as in the FD-KEH comparison with $\mathcal{N}[\Psi] = |\nabla\Psi|^2$, $\lambda = 3$.

Table 1. A comparison of code output for scalar models. The values in the table give the percent rms difference between of Ψ -values from three numerical methods as in Figure 1. The rms differences were computed from the points along each principal axis.

	Source axis	Perp. axis	Rotation axis
Linear ($\mathcal{N}[\Psi] = 0$)			
FD to KEH	0.25	0.24	0.10
FD to ES	1.02	1.09	1.08
ES to KEH	1.07	1.15	1.11
$\mathcal{N}[\Psi] = \Psi^3$, $\lambda = 100$			
FD to KEH	3.56	3.44	0.21
FD to ES	1.22	1.67	1.14
ES to KEH	3.28	2.86	1.19
$\mathcal{N}[\Psi] = \Psi^3$, $\lambda = -2.2$			
FD to KEH	0.35	0.36	0.21
FD to ES	1.96	2.02	2.08
ES to KEH	1.77	1.99	1.92
$\mathcal{N}[\Psi] = \nabla\Psi ^2$, $\lambda = 3$			
FD to KEH	1.73	1.47	1.33
FD to ES	1.39	1.80	1.44
ES to KEH	2.69	2.76	2.77
$\mathcal{N}[\Psi] = \nabla\Psi ^2$, $\lambda = -100$			
ES to KEH	1.96	2.20	1.65
$\mathcal{N}[\Psi] = \Psi\Box\Psi$, $\lambda = -0.7$			
FD to KEH	0.53	0.48	0.20
FD to ES	1.06	1.13	1.13
ES to KEH	0.99	1.23	1.00

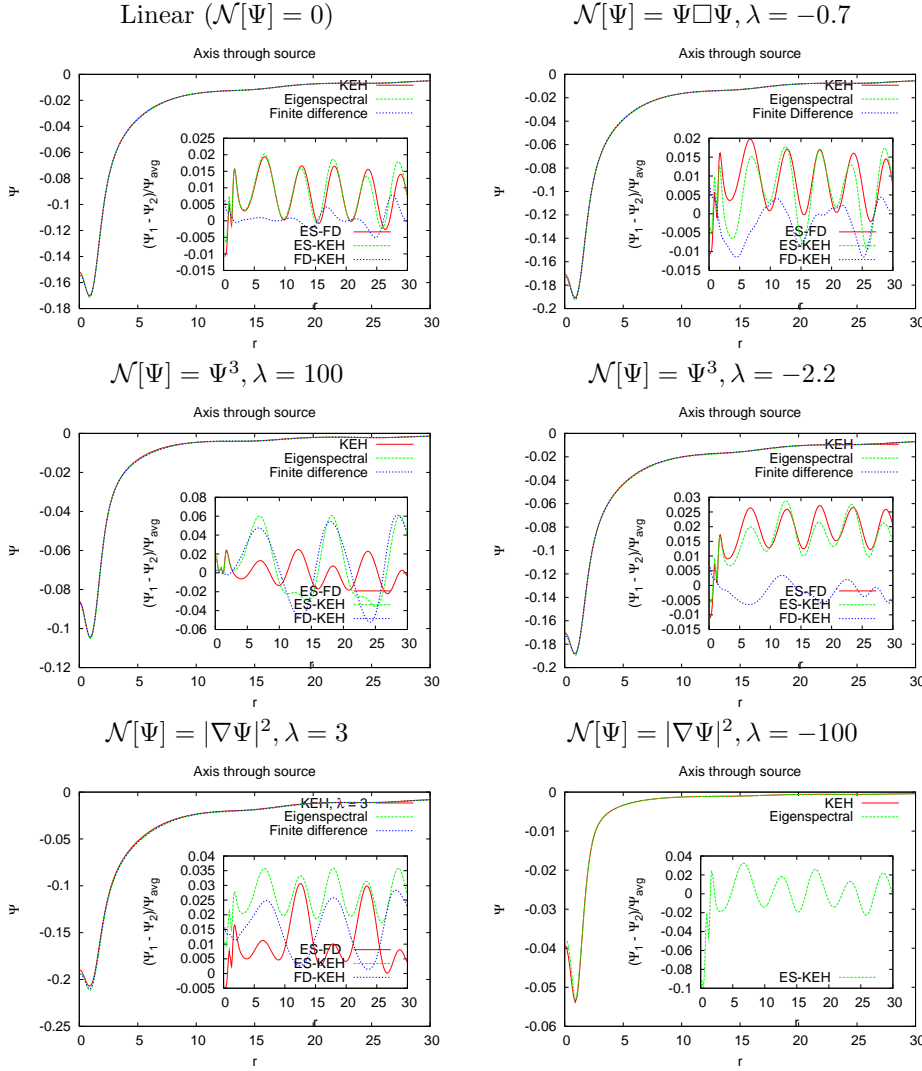


Figure 2. The scalar field Ψ as a function of distance r from the origin in units of the orbital radii along the source axis. Each panel corresponds to a model specified by the form of the nonlinear term $\mathcal{N}[\Psi]$ and the value of the parameter λ , as written above the panels. In all cases, the angular frequency of rotation is $\Omega = 0.3$ and the source strengths are unity. The plots show results from the KEH method (solid red curves), the Eigenspectral method (dashed green) and the Finite Difference code (dotted blue). The insets give more detailed comparisons between these results; the curves show the difference between pairs of solutions relative to the average field. The Eigenspectral method gives a stronger periodic modulation relative to the other methods, due to its restriction to low-order harmonics.

Table 2. The range of nonlinear amplitude λ in scalar models for which codes converged. The first column gives the type of nonlinearity, while the second column indicates the numerical method, as discussed in the text. The third and fourth columns, showing λ_{\min} and λ_{\max} , give the range of λ for which convergence was achieved. Where an inequality is given, no limiting value was found.

$\mathcal{N}[\Psi]$	Code	λ_{\min}	λ_{\max}
Ψ^3	KEH	-2.3	11
Ψ^3	KEH, softened/continued	-2.3	>10000
Ψ^3	FD	-2.5	>1000
Ψ^3	ES	-2.4	>1000
$ \nabla\Psi ^2$	KEH	-30	7.7
$ \nabla\Psi ^2$	KEH, softened/continued	<-1000	7.7
$ \nabla\Psi ^2$	FD	-2.0	5.6
$ \nabla\Psi ^2$	ES	-360	7.3
$ \nabla\Psi ^2$	ES, continued	<-1000	7.3
$\Psi\square\Psi$	KEH	-0.96	1.3
$\Psi\square\Psi$	KEH, softened/continued	-0.96	10
$\Psi\square\Psi$	FD	-1.8	>1000
$\Psi\square\Psi$	ES	-1.7	>1000

4. Measuring range of convergence

For each code, a series of runs varying the nonlinear amplitude λ determines the range of λ for which the code gives a convergent solution. The source distribution and boundary location are fixed.

Softening and continuation are used to extend the maximum absolute value of λ that allows convergence. For each nonlinear term, strikingly different behaviour is found for opposite signs of λ . That is, denoting by λ_{\max} and λ_{\min} the largest positive value and the smallest negative value of λ for which a code converges, we find for each nonlinear term that λ_{\max} and $|\lambda_{\min}|$ differ by at least a factor of 100. In each case, the sign of λ that yields greatest convergence is opposite to the sign of the source term, where the source is large. The ‘favorable’ sign damps the effect of the source distribution on the field, while the ‘unfavorable’ sign gives an amplified effective source. For $\mathcal{N}[\Psi] = \Psi^3, |\nabla\Psi|^2, \Psi\square\Psi$, the favorable signs of lambda are +, -, +, respectively.

Softening and continuation improved the range of convergence for the favorable sign, but had no effect on the limit of the unfavorably signed λ . Figure 3 shows the effect of softening, parametrized by ω , and of using continuation on the limiting favorable-sign values of λ .

Convergence is attained, when softening and continuation are used, for all attempted favorable sign values for λ , except when using the KEH method with the $\Psi\square\Psi$ nonlinear term or when using the Finite Difference method with the $|\nabla\Psi|^2$ nonlinear term.

The range of convergence results are given in Table 2. If softening and continuation maintain convergence to the largest tested value of λ , the uncertainty in the true maximum value or minimum value of λ is indicated by $>$ or $<$.

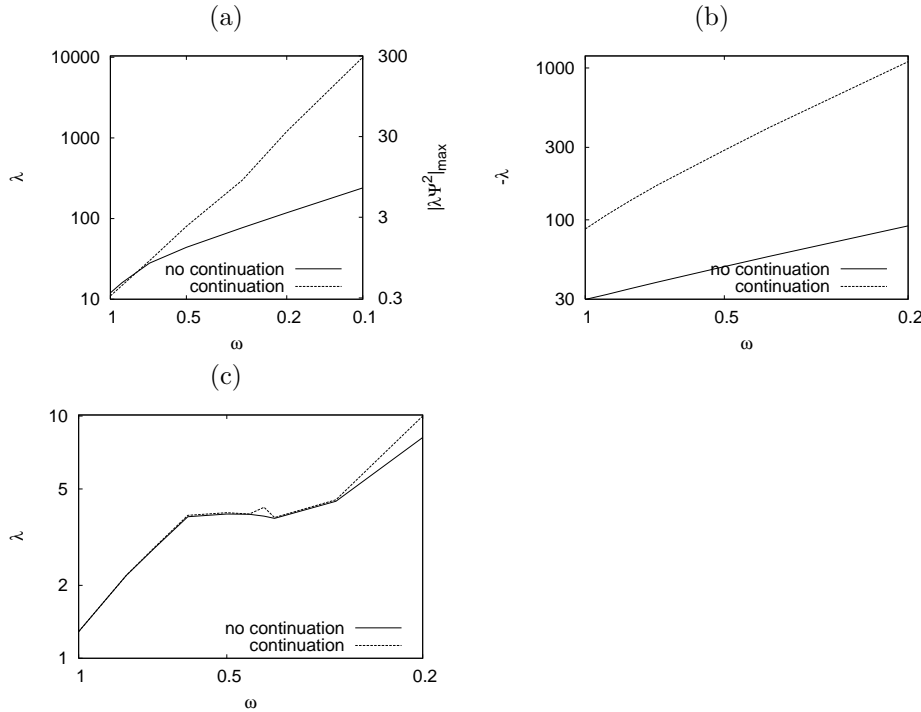


Figure 3. The effect of a softening parameter ω and continuation on range of λ . The plots indicate the limiting value of λ for convergence of the KEH code. Each panel corresponds to a different nonlinear model, with $\mathcal{N}[\Psi]$ set to Ψ^3 (panel a), $|\nabla\Psi|^2$ (panel b), and $\Psi\Box\Psi$ (panel c). In each case, the limiting λ value of the opposite sign was unaffected by softening or continuation.

4.1. Boundary and convergence

As described in Sect. 6 below, Uryu has obtained a convergent helically symmetric BNS code within a region that extends about one wavelength from the center of the source, by using a waveless formulation outside that radius. Led by this result, we explored the effects of the outer boundary placement on the range of converging λ for the fully helical code.

While bringing the boundary in has little effect on the limits of the favorably signed λ , it does allow a significantly larger magnitude of the unfavorable λ , as shown in Fig. 4.

5. Hybrid helical/waveless equations

One expects a helically symmetric solution Ψ to accurately approximate the outgoing solution only in the near zone, where the Coulomb part of the field is dominant. That is, the two solutions agree when one can ignore the wavelike character of Ψ . In that situation, one should be able to approximate the outgoing solution with comparable accuracy by using a waveless approximation in which only the Coulomb part of the field is retained. We can obtain an approximation of this kind by replacing the D'Alembertian by the Laplacian – by discarding second time derivatives. In

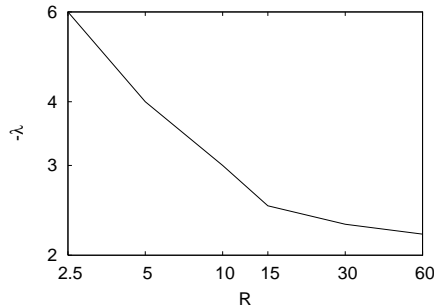


Figure 4. The effect of the outer boundary R on convergence in the cubic nonlinear model ($\mathcal{N}[\Psi] = \Psi^3$). The limiting value of λ for which the KEH method converges as a function of outer boundary location, R , in units of orbital radii.

the last part (5.1) of this Section, we compare results of this version of a waveless approximation to a solution that has exact helical symmetry. We impose equivalent boundary conditions on the solutions by imposing helical symmetry only in the near zone, in effect matching to an exterior waveless solution. As we describe Sect. 6, in Uryu’s neutron-star code, a helically symmetric near-zone is similarly matched on an initial hypersurface to an exterior waveless solution to the Einstein-Euler equations.

We find as follows a helically symmetric near-zone Ψ matched to an exterior waveless solution. As before, after imposing helical symmetry, we have a scalar equation for the toy scalar model in the form

$$(\nabla^2 - \Omega^2 \partial_\varphi^2) \Psi = S + \lambda \mathcal{N}[\Psi], \quad (26)$$

where the effective source is a sum of the inhomogeneous source term and a nonlinear source. Instead of inverting the operator on the left hand side in the equation with the wavelike Green’s function \mathcal{L}^{-1} of Eq. (6), we split the operator, writing

$$\nabla^2 \Psi = S + \lambda \mathcal{N}[\Psi] + \Omega^2 \partial_\varphi^2 \Psi. \quad (27)$$

We regard the extra term on the right hand side as a part of the effective source, and invert the Laplacian operator to solve iteratively for Ψ .

We can now truncate the extra source term $\Omega^2 \partial_\varphi^2 \Psi$ (as in Uryu et al.[10]) at some radius R_{trunc} written in units of the wavelength π/Ω of the quadrupole wave. The resulting solution is helically symmetric inside the truncation radius and waveless outside.

If this truncation radius is too large, the iteration fails to converge. In fact, this iterative method, in which we invert the Laplacian instead of the full second-order operator, fails to converge even for nonlinear terms that yield convergent solutions when we impose helical symmetry everywhere and use the iterative methods of the previous section. For a given small truncation radius, the critical value of λ depends on the outer boundary radius R_{out} , as in the fully helical result of Figure 4.

In Fig. 5, we plot the critical value $|\lambda_{\text{min}}|$ of λ as a function of R_{trunc} , for the nonlinear term $\lambda \Psi^3$ with the unfavorable sign choice for λ . As in the models discussed above, the inhomogeneous source term is the double Gaussian, with $\Omega = 0.3$. In the upper panel, we plot results of iteration without continuation. Different curves correspond to different value of outer boundary radius, R_{out} . As is clear from the figure, the value $\lambda_{\text{cr}} = \lambda_{\text{min}}$ is nearly independent of R_{trunc} up to maximum value of

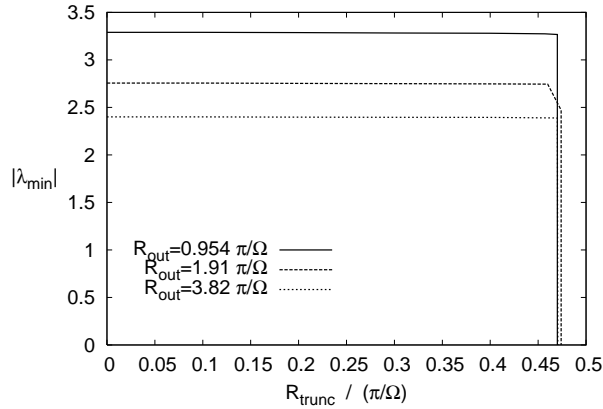


Figure 5. Critical parameter $|\lambda_{\min}|$ is plotted as a function of R_{trunc} . We plot curves for different computational outer boundaries R_{out} . Note that R_{trunc} is normalized by π/Ω . The range of convergence is given for the iterative method described in this section with continuation used to reach a limiting value of $|\lambda_{\min}|$.

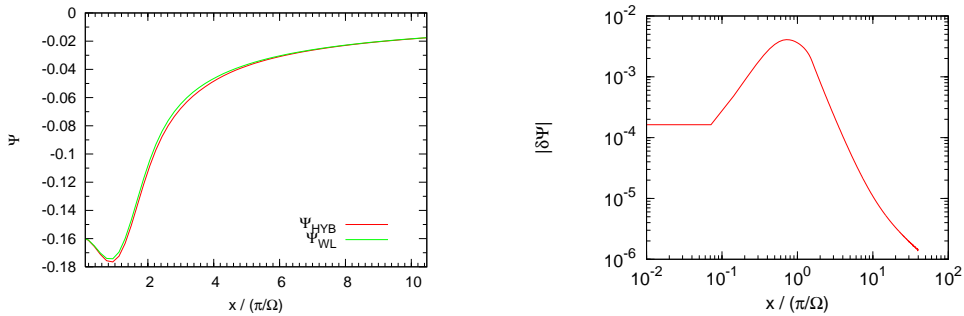


Figure 6. Left panel: Plot of hybrid (Ψ_{HYB}) and waveless (Ψ_{WL}) solutions along the source axis normalized by π/Ω , the wavelength of the $l = m = 2$ mode. Right panel: The absolute error between hybrid and waveless solutions along the same axis.

R_{trunc} . Beyond that value, the iteration based on inverting the Laplacian does not converge for any finite value of λ . This transition from convergence to non-convergence is abrupt, and we see a clear limit, $R_{\text{trunc}} \sim 0.47$, for the truncation radius. We also see that using continuation we reached an absolute limit of $R_{\text{trunc}} \sim 0.47$ for any value of R_{out} .

We note that the truncation radius of the extra source (that is, $\Omega^2 \partial_\varphi^2 \Psi$) cannot be larger than a half of wave length of quadrupole component of wave. This is roughly consistent with the results of Uryu's code described below.

5.1. Comparing hybrid and waveless results

In Fig. 5.1 we plot the difference between a hybrid solution and a solution that is fully waveless. The profile is along the source (along the x -axis). The resulting similarity of the solutions confirms our expectation that waveless and helically symmetric solutions should agree in the near zone. The level of disagreement, between 0.05 and 2%, for

r less than one wavelength, appears primarily to result from the fact that the two solutions do not have identical boundary values at the boundary R_{trunc} of the region where one solution is helically symmetric and the other is waveless. That is, by truncating the ∂_ϕ^2 term in the effective source at $r = R_{\text{trunc}}$, we match the helically symmetric solution to an exterior waveless solution, but to a slightly different waveless solution than that obtained by using the waveless equation everywhere.

6. Helically symmetric binary neutron star code

In this section, we report the construction of a first helically symmetric code for binary neutron stars. The code modifies a recently developed numerical method for computing models of compact binary stars in a waveless approximation [10] to produce solutions to the full Einstein-Euler system (the Einstein-perfect fluid equations) with exact helical symmetry. Waveless and helically symmetric solutions are expected to be accurate in the near zone, where the gravitational wave amplitude is small compared to the Coulomb contribution to each metric potential; and in its present form, the helically symmetric code converges only in the near zone. Convergence of the code is achieved by using the waveless formulation outside one wavelength. In effect, the outer waveless solution imposes boundary conditions on the helically symmetric solution at the edge of the near zone.

6.1. Formulation

Our formulation is applied to Einstein's equation written in 3+1 form, with spacetime $\mathcal{M} = \mathbb{R} \times \Sigma$. Let n^α be the future-pointing unit vector normal to the slices $\{t\} \times \Sigma$ of this foliation. The generator of the time coordinate t^α and the helical symmetry vector $k^\alpha = t^\alpha + \Omega\phi^\alpha$ are related to n^α and the shift β^α in the usual way,

$$t^\alpha = \alpha n^\alpha + \beta^\alpha \quad \text{and} \quad k^\alpha = \alpha n^\alpha + \omega^\alpha, \quad (28)$$

where ω^α is a rotating shift vector $\omega^\alpha = \beta^\alpha + \Omega\phi^\alpha$.

The projection 4-tensor $\gamma_{\alpha\beta}$ orthogonal to n_α , defined by

$$\gamma_{\alpha\beta} = g_{\alpha\beta} + n_\alpha n_\beta, \quad (29)$$

is associated with the 3-metrics $\gamma_{ab}(t)$ on the spatial slices Σ_t . (Any spatial tensor on Σ_t can be identified with a spacetime tensor orthogonal to n^α on all its indices). The metric then has the form,

$$ds^2 = -\alpha^2 dt^2 + \gamma_{ij}(dx^i + \beta^i dt)(dx^j + \beta^j dt). \quad (30)$$

The extrinsic curvature of each slice Σ is defined by

$$K_{ab} = -\frac{1}{2}\mathcal{L}_n\gamma_{ab}, \quad (31)$$

where \mathcal{L}_n operating on spatial tensors such as γ_{ab} has the meaning

$$\mathcal{L}_n\gamma_{ab} := \frac{1}{\alpha}\partial_t\gamma_{ab} - \frac{1}{\alpha}\mathcal{L}_\beta\gamma_{ab}, \quad (32)$$

with $\partial_t\gamma_{ab}$ the pullback of $\mathcal{L}_t\gamma_{\alpha\beta}$ to Σ . We introduce a conformal decomposition of the spatial metric, $\gamma_{ab} = \psi^4\tilde{\gamma}_{ab}$, and a condition $\tilde{\gamma} = f$, where f is the determinant of the flat metric f_{ab} and $\tilde{\gamma}$ the determinant of the conformal metric $\tilde{\gamma}_{ab}$. Further h_{ab} and h^{ab} are introduced by

$$\tilde{\gamma}_{ab} = f_{ab} + h_{ab}, \quad \tilde{\gamma}^{ab} = f^{ab} + h^{ab}. \quad (33)$$

Helical symmetry, $\mathcal{L}_k g_{\alpha\beta} = 0$, implies for the 3-metric and extrinsic curvature,

$$\mathcal{L}_k \gamma_{ab} = 0, \quad \mathcal{L}_k K_{ab} = 0. \quad (34)$$

Using the relation (28) between n^α and k^α , we have

$$\mathcal{L}_n \gamma_{ab} = -\frac{1}{\alpha} \mathcal{L}_\omega \gamma_{ab}, \quad \text{and} \quad \mathcal{L}_n K_{ab} = -\frac{1}{\alpha} \mathcal{L}_\omega K_{ab}. \quad (35)$$

Projections of the Einstein equation along the normal n^α are the Hamiltonian and momentum constraints,

$$(G_{\alpha\beta} - 8\pi T_{\alpha\beta}) n^\alpha n^\beta = 0, \quad (36)$$

$$(G_{\alpha\beta} - 8\pi T_{\alpha\beta}) \gamma_a^\alpha n^\beta = 0. \quad (37)$$

while the spatial projection has trace and tracefree part

$$(G_{\alpha\beta} - 8\pi T_{\alpha\beta}) \gamma^{\alpha\beta} = 0, \quad (38)$$

$$(G_{\alpha\beta} - 8\pi T_{\alpha\beta}) \left(\gamma_a^\alpha \gamma_b^\beta - \frac{1}{3} \gamma_{ab} \gamma^{\alpha\beta} \right) = 0. \quad (39)$$

The above set of equations are solved for the conformal factor ψ , the shift β^a , the lapse α and the deviation of the conformal metric from the flat metric h_{ab} , respectively, imposing coordinate conditions, the maximal slicing condition, $K = 0$, and the generalized Dirac condition $\overset{\circ}{D}_b \tilde{\gamma}^{ab} = 0$, as in the waveless formulation [11]. In the following section, we concentrate on the treatment of the spatially tracefree part of Einstein equation (39), solved for h_{ab} , in which the second time derivatives of h_{ab} change the equation from elliptic (in the waveless formulation) to the mixed form that characterizes helically symmetric wave equations. A concrete treatment of the other components of the field equations that yield elliptic equations for ψ , β^a , and α , as well as equations of matter source is given in Ref. [11].

The waveless code differs from the helically symmetric code by the requirement that $\tilde{\gamma}_{ab}$ have vanishing derivative along t^α instead of vanishing derivative along k^α . The extrinsic curvature and matter variables are still required to be helically symmetric. These requirements result in elliptic equations for the field variables, including the non-conformal part of the 3-metric $h_{ab} = \tilde{\gamma}_{ab} - f_{ab}$.

In the helically symmetric code, with $\partial_t \tilde{\gamma}_{ab}$ nonzero, the elliptic equations are replaced by Helmholtz equations for h_{ab} , whose source is almost identical to that of the waveless formulation. We implement a KEH solver for the helical formulation and investigate convergence of the iteration for a compact binary star source.

6.2. Helmholtz equation for h_{ab}

Eq. (39) has the form

$$(G_{\alpha\beta} - 8\pi T_{\alpha\beta}) \left(\gamma_a^\alpha \gamma_b^\beta - \frac{1}{3} \gamma_{ab} \gamma^{\alpha\beta} \right) = \mathcal{E}_{ab} - \frac{1}{3} \gamma_{ab} \gamma^{cd} \mathcal{E}_{cd} = 0, \quad (40)$$

where

$$\mathcal{E}_{ab} := -\mathcal{L}_n K_{ab} + {}^3R_{ab} + K K_{ab} - 2K_{ac} K_b^c - \frac{1}{\alpha} D_a D_b \alpha - 8\pi S_{ab}, \quad (41)$$

with ${}^3R_{ab}$ the Ricci tensor on Σ associated with γ_{ab} , and S_{ab} the projection of the energy stress tensor, $S_{ab} := T_{\alpha\beta} \gamma_a^\alpha \gamma_b^\beta$.

By isolating the terms, $\square h_{ab} := (-\partial_t^2 + \overset{\circ}{D}^c \overset{\circ}{D}_c) h_{ab}$, that occur in \mathcal{E}_{ab} in Eq. (41), one can rewrite Eq. (40) in the form

$$\square h_{ab} = \mathcal{S}_{ab}, \quad (42)$$

where \square is the flat d'Alembertian operator and $\overset{\circ}{D}^a := f^{ab} \overset{\circ}{D}_b$. Then, as in the scalar models, helical symmetry of the conformal metric, $\mathcal{L}_k \tilde{\gamma}_{ab} = \mathcal{L}_k h_{ab} = 0$, results in the operator

$$\square h_{ab} = -\partial_t^2 h_{ab} + \overset{\circ}{D}^c \overset{\circ}{D}_c h_{ab} = (\overset{\circ}{\Delta} - \Omega^2 \mathcal{L}_\phi^2) h_{ab}, \quad (43)$$

where the flat Laplacian is defined by $\overset{\circ}{\Delta} = \overset{\circ}{D}^c \overset{\circ}{D}_c$.

Even when one uses the Cartesian components h_{ij} of h_{ab} , however, $\overset{\circ}{\Delta} - \Omega^2 \mathcal{L}_\phi^2$ does not coincide with the Helmholtz operator, because $\partial_\phi h_{ij}$ is a Cartesian component of $\phi \cdot \overset{\circ}{\mathbf{D}} h_{ab}$, not of $\mathcal{L}_\phi h_{ab}$. To isolate the Helmholtz operator $\mathcal{L} = \overset{\circ}{\Delta} - \Omega^2 \partial_\phi^2 = \overset{\circ}{\Delta} - \Omega^2 (\phi \cdot \overset{\circ}{\mathbf{D}})^2$, we write $\partial_\phi := \phi \cdot \overset{\circ}{\mathbf{D}}$ and find

$$\mathcal{L}_\phi^2 \tilde{\gamma}_{ab} = \partial_\phi^2 \tilde{\gamma}_{ab} + (\partial_\phi \tilde{\gamma}_{ac} + \mathcal{L}_\phi \tilde{\gamma}_{ac}) \overset{\circ}{D}_b \phi^c + (\partial_\phi \tilde{\gamma}_{cb} + \mathcal{L}_\phi \tilde{\gamma}_{cb}) \overset{\circ}{D}_a \phi^c, \quad (44)$$

where a relation $\phi^c \overset{\circ}{D}_c (\overset{\circ}{D}_a \phi^b) = 0$ is used. Moving all terms in Eq. (44) except $\partial_\phi^2 \tilde{\gamma}_{ab}$ from the LHS to the RHS of Eq. (42), we obtain the Helmholtz form

$$\begin{aligned} \mathcal{L} h_{ab} = \bar{\mathcal{E}}_{ab} := & 2 \left(\bar{\mathcal{E}}_{ab} - \frac{1}{3} \tilde{\gamma}_{ab} \tilde{\gamma}^{cd} \bar{\mathcal{E}}_{cd} \right) \\ & - \frac{1}{3} \tilde{\gamma}_{ab} \overset{\circ}{D}^e h^{cd} \overset{\circ}{D}_e h_{cd} + \frac{1}{3} \tilde{\gamma}_{ab} \Omega^2 \partial_\phi h^{cd} \partial_\phi h_{cd}, \end{aligned} \quad (45)$$

where the barred expression $\bar{\mathcal{E}}_{ab}$ is defined by

$$\begin{aligned} \bar{\mathcal{E}}_{ab} := & R_{ab}^{\text{NL}} + {}^3\tilde{R}_{ab}^\psi - \frac{1}{\alpha} D_a D_b \alpha - 2\psi^4 \tilde{A}_{ac} \tilde{A}_b{}^c - 8\pi S_{ab} \\ & + \frac{1}{2} \left(\frac{\psi^4}{\alpha^2} - 1 \right) \Omega^2 \partial_\phi^2 h_{ab} + \frac{\psi^4}{\alpha^2} \Omega \left(\mathcal{L}_\phi \mathcal{L}_\beta \tilde{\gamma}_{ab} + \frac{1}{2} \mathcal{L}_{[\beta, \phi]} \tilde{\gamma}_{ab} \right) \\ & + \frac{\psi^4}{2\alpha^2} \Omega^2 \left[(\partial_\phi \tilde{\gamma}_{ac} + \mathcal{L}_\phi \tilde{\gamma}_{ac}) \overset{\circ}{D}_b \phi^c + (\partial_\phi \tilde{\gamma}_{cb} + \mathcal{L}_\phi \tilde{\gamma}_{cb}) \overset{\circ}{D}_a \phi^c \right] \\ & + \frac{\psi^4}{2\alpha^2} \mathcal{L}_\beta \mathcal{L}_\beta \tilde{\gamma}_{ab} + \frac{\psi^4}{\alpha} \tilde{A}_{ab} \mathcal{L}_\omega \ln \frac{\psi^8}{\alpha}. \end{aligned} \quad (46)$$

In this expression for $\bar{\mathcal{E}}_{ab}$, the coordinate conditions $K = 0$ and $\overset{\circ}{D}_b \tilde{\gamma}^{ab} = 0$, mentioned above, are imposed; and the tracefree part A_{ab} of the extrinsic curvature, $A_{ab} := K_{ab} - \frac{1}{3} \gamma_{ab} K$, is introduced in the rescaled form $\tilde{A}_{ab} := \psi^{-4} A_{ab}$. Terms R_{ab}^{NL} and ${}^3\tilde{R}_{ab}^\psi$ arise from the conformal decomposition of the Ricci tensor [11].

The source (46) can be written concisely without separating the second derivative term $\partial_\phi^2 h_{ab}$ explicitly as above. Applying the helical symmetry condition (35) to Eq. (41) and subtracting $\partial_\phi^2 h_{ab}$ term from both side of Eq. (40), the source term of the exactly helical equation Eq. (45) can be rewritten

$$\begin{aligned} \bar{\mathcal{E}}_{ab} := & \frac{1}{\alpha} \mathcal{L}_\omega (\psi^4 \tilde{A}_{ab}) - \frac{1}{2} \Omega^2 \partial_\phi^2 h_{ab}, \\ & + R_{ab}^{\text{NL}} + {}^3\tilde{R}_{ab}^\psi - \frac{1}{\alpha} D_a D_b \alpha - 2\psi^4 \tilde{A}_{ac} \tilde{A}_b{}^c - 8\pi S_{ab} \end{aligned} \quad (47)$$

which is equivalent to the above source term (46).

6.3. A different formulation for the use of elliptic solver, and a comparison with the waveless approximation

Instead of isolating the Helmholtz operator on the LHS for the case of helical symmetry, one can formally isolate an elliptic operator and solve the equation iteratively using an elliptic solver as in the waveless approximation. With this grouping of terms, the helical symmetry condition (35), applied to Eq. (41), leaves the term $\mathcal{L}_\omega K_{ab}$ as part of the effective source, and the Laplacian of h_{ab} is separated out from ${}^3R_{ab}$. With gauge conditions $K = 0$ and $\mathring{D}_b \tilde{\gamma}^{ab} = 0$, as before, we have

$$\mathring{\Delta} h_{ab} = 2 \left(\widehat{\mathcal{E}}_{ab} - \frac{1}{3} \tilde{\gamma}_{ab} \tilde{\gamma}^{cd} \widehat{\mathcal{E}}_{cd} \right) - \frac{1}{3} \tilde{\gamma}_{ab} \mathring{D}^e h^{cd} \mathring{D}_e h_{cd}, \quad (48)$$

where $\widehat{\mathcal{E}}_{ab}$ is given by

$$\widehat{\mathcal{E}}_{ab} := \frac{1}{\alpha} \mathcal{L}_\omega(\psi^4 \tilde{A}_{ab}) + R_{ab}^{\text{NL}} + {}^3\tilde{R}_{ab}^\psi - \frac{1}{\alpha} D_a D_b \alpha - 2\psi^4 \tilde{A}_{ac} \tilde{A}_b{}^c - 8\pi S_{ab}. \quad (49)$$

In Eq.(49), the first term appears instead of the last three lines in Eq. (46).

We find that the helically symmetric code does not converge in this method when we solve the above set of equations on Σ with a boundary that extends several wavelengths (or more) beyond the source. We were, however, able to obtain a converged solution when exact helical symmetry is imposed only in the near zone, within about a wavelength from the source, and the waveless approximation is used for larger r , effectively setting boundary conditions at the boundary of the helically symmetric inner zone. In a waveless approximation [11], the time derivative of the conformal metric, $\partial_t \tilde{\gamma}_{ab}$ is assumed to be zero. As a result the extrinsic curvature is associated with the nonrotating shift β^a ,

$$K_{ab} = -\frac{1}{2} \mathcal{L}_n \gamma_{ab} = \frac{1}{2\alpha} \mathcal{L}_\beta \gamma_{ab}, \quad (50)$$

instead of the rotating shift ω^a as in (35).

In the next section, we compare the near-zone helically symmetric solution to a solution that is everywhere waveless. For the near-zone helically symmetric solution, the change from helical symmetry to the waveless formulation at about one wavelength from the source implies for K_{ab} the condition

$$K_{ab} = \begin{cases} \frac{1}{2\alpha} \mathcal{L}_\omega \gamma_{ab} = \frac{1}{2\alpha} (\mathcal{L}_\beta \gamma_{ab} + \Omega \mathcal{L}_\phi \gamma_{ab}), & \text{for } r < f \frac{\pi}{\Omega}, \\ \frac{1}{2\alpha} \mathcal{L}_\beta \gamma_{ab} + \frac{1}{3\alpha} \gamma_{ab} D_c (\Omega \phi^c), & \text{for } r \geq f \frac{\pi}{\Omega}, \end{cases} \quad (51)$$

where π/Ω is the approximate wavelength of the $l = m = 2$ gravitational wave mode. The constant f , the coordinate radius of the helically symmetric zone in units of π/Ω , is restricted to $f \lesssim 1$ for convergence.

6.4. Numerical code

Our numerical code is based on the finite difference code developed in Refs. [12, 10]. The code extends a KEH iteration scheme to the binary neutron star computation. Cartesian components of the field equations are solved numerically on spherical coordinate grids, r , θ , and ϕ . An equally spaced grid is used from the center of orbital motion to $5R_0$ where there are 16 or 24 grid points per R_0 ; from $5R_0$ to the outer boundary of computational region a logarithmically spaced grid has 60 or 90,

where R_0 is the coordinate radius of a compact star along a line passing through the center of orbit to the center of a star. Accordingly, for θ and ϕ there are 32 or 48 grid points each from 0 to $\pi/2$ and multipoles are summed up to $l = 32$ [12].

6.5. Numerical solution

In this section we present results of our code for a binary system modeled by a perfect fluid having polytropic equation of state, $p = K\rho^\Gamma$, with ρ the baryon density. We display results for the choices $\Gamma = 2$, appropriate to neutron star matter; for compactness of a star in isolation $(M/R)_\infty = 0.14$; and for half the binary separation $d/R_0 = 1.375$. Solutions with helical symmetry are not uniquely specified by this choice of parameters and equation of state. Because they are stationary solutions with equal amounts of ingoing and outgoing waves, they are not asymptotically flat, and one must find an appropriate choice of boundary conditions. As discussed in the Consortium papers, one seeks conditions that minimize the amplitude of gravitational waves. In toy models discussed above, conditions are fixed by the choice of a half-advanced plus half-retarded Green function at each iteration. In solving the Einstein equation, however, convergence is achieved only in the near zone, and, as we have emphasized, we impose boundary conditions by matching to an exterior waveless solution outside a coordinate radius $f\pi/\Omega$.

For $f \lesssim 1$, the code converges, yielding a helically symmetric solution in the near zone $r \leq f\pi/\Omega$. As shown in Fig. 7, the solution is *nearly identical* to the waveless solution. The right panel shows a difference larger than 1% only when the metric component itself is smaller than 0.03; as a percentage of $h_{ij}(r = 0)$, the difference is everywhere less than 1%. The threshold of the value of f for convergence is $0.7 \lesssim f \lesssim 1$ depending on the binary separation, compactness and resolution of finite differencing. We may expect from the result that, with boundary conditions that minimize the amplitude of gravitational waves, the exact helical solution will be close to the waveless solution near the source. This is a hopeful outcome: The waveless and helically symmetric formalisms are each intended to give a solution whose inaccuracy arises from neglecting gravitational waves, and they should give nearly identical results in the near zone where the gravitational wave amplitude is small compared to the Coulomb fields.

In modeling binary neutron stars comparable accuracy is likely to result from codes that match a helically symmetric solution to a waveless solution, from a purely waveless code, and from a helically symmetric code. From a more mathematical perspective, however, finding a solution that has exact helical symmetry on the full spacetime is an appealing goal. In the neutron star code, we have isolated a set of nonlinear terms that appear responsible for divergence outside the near zone. Improvement of the convergence of the code is required to extend the matching radius beyond a few wavelengths, which may involve a use of metric components in spherical instead of Cartesian coordinates. Further investigation of this alternative is a subject of our future work.

Acknowledgments

This work was supported in part by NSF Grant PHY 0503366 and NASA Grant NNG05GB99G. SY has been supported in part by Charles E. Schmidt College of

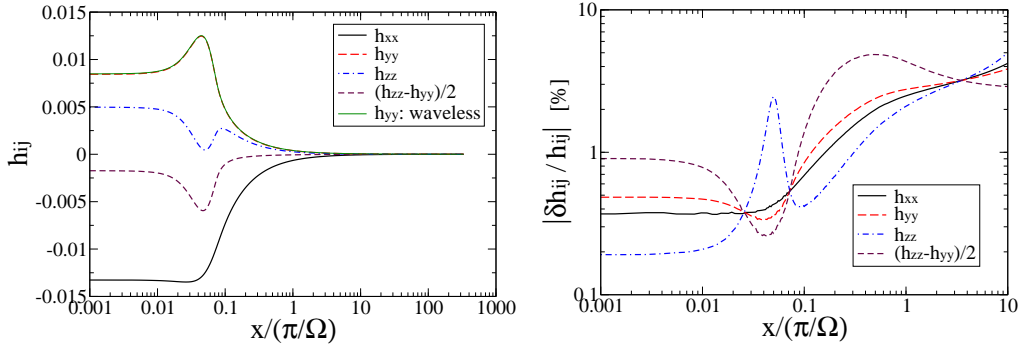


Figure 7. Left panel: Plot of components h_{ij} along the x -axis normalized by π/Ω , the wavelength of the $l = m = 2$ mode. The solution to Eq. (48) with the mixed helical and waveless source of Eqs. (49) and (51), and the h_{yy} component of the waveless solution are shown. Right panel: The fractional difference of these two solutions is plotted for selected components of h_{ij} for $r < 10\pi/\Omega$. The fractional differences increase for larger r because the values of the components h_{ij} are themselves small. A compact star extends from $x/(\pi/\Omega) = 0.0125$ to 0.079 , the boundary of computational region is set to $10^4 R_0 \sim 332\pi/\Omega$, and the cutoff constant f in Eq. (51) is set to $f = 0.7$.

Science at FAU. We thank Chris Beetle, Richard Price, Eric Gourgoulhon, Francois Limousin, and Masaru Shibata for helpful discussions.

References

- [1] J. L. Friedman, K. Uryū and M. Shibata, *Phys. Rev. D* **65**, 064035 (2002).
- [2] E. Gourgoulhon, P. Grandclement, and S. Bonazzola, *Phys. Rev. D* **65**, 044020 (2002).
- [3] J. K. Blackburn and S. Detweiler, *Phys. Rev. D* **46**, 2318 (1992). S. Detweiler, *Phys. Rev. D* **50**, 4929 (1994).
- [4] J.T. Whelan, W. Krivan, and R.H. Price, *Class. Quant. Grav.* **17**, 4895 (2000)
- [5] J.T. Whelan, C. Beetle, W. Krivan, and R.H. Price, *Class. Quant. Grav.* **19**, 1285 (2002).
- [6] R. H. Price, *Class. Quant. Grav.* **21**, S281 (2004)
- [7] Z. Andrade, C. Beetle, A. Blinov, B. Bromley, L.M. Burko, M. Cranor, R. Owen and R.H. Price, *Phys. Rev. D* **70**, 064001 (2004).
- [8] C. G. Torre, *J. Math. Phys.* **44**, 6223 (2003).
- [9] B. Bromley, R. Owen, and R.H. Price, *Phys. Rev. D* **71**, 104017 (2005).
- [10] K. Uryū, F. Limousin, J. L. Friedman, E. Gourgoulhon, M. Shibata, “Binary compact stars in a waveless approximation”, preprint (gr-qc/0511136).
- [11] M. Shibata, K. Uryū, and J. L. Friedman, *Phys. Rev. D* **70**, 044044 (2004); Erratum *ibid.* **70**, 129901 (2004).
- [12] K. Uryū and Y. Eriguchi, *Phys. Rev. D* **61**, 124023 (2000).